ACTA IMEKO
ISSN: 2221-870X
December 2026, Volume 15, Number 4, 1 - 10

Visible-to-terahertz integrated 2D and 3D imaging of surface and subsurface features in a fresco mock-up

Emma Vannini[1,2,3], Ilaria Catapano[4], Alice Dal Fovo[1], Valentina di Sarno[5], Alessandra Rocco[5], Pasquale Maddaloni[5], Raffaella Fontana[1]

[1] *National Research Council – National Institute of Optics (CNR-INO), Largo E. Fermi 6, 50125 Firenze, Italy*
[2] *Department of Physics and Astronomy, University of Florence, Via Sansone 1, 50019 Sesto Fiorentino (FI), Italy*
[3] *Department of Computer Science, University of Verona, Strada le Grazie 15, 37134 Verona, Italy*
[4] *National Research Council – Institute for Electromagnetic Sensing of the Environment (CNR-IREA), Via Diocleziano 328, 80124 Pozzuoli (NA), Italy*
[5] *National Research Council – National Institute of Optics (CNR-INO), Via Campi Flegrei 34, 80078 Pozzuoli (NA), Italy*

ABSTRACT
The stratigraphy of mural paintings consists of a complex sequence of plaster layers characterized by progressively finer aggregates. This multilayered structure is highly susceptible to deterioration at different depths, making the detection of subsurface defects and hidden features essential for accurate conservation assessments. Infrared (IR) and Terahertz (THz) radiation can penetrate the surface, providing valuable information on subsurface conditions. In this study, a multi-technique survey was conducted on a purpose-built mock-up using Near-Infrared (NIR) reflectography, active thermography in both the Mid-Wave (MWIR) and Long-Wave (LWIR) infrared ranges, Terahertz Time-Domain Imaging (THz-TDI), and optical scanning microprofilometry. The latter was employed to generate 3D models of the surface morphology with micrometric precision. The topographic data serve as a reference framework, enabling the effective discrimination of anomalies in IR and THz signals arising from surface morphology. The results illustrate the capabilities and limits of each technique in detecting subsurface features and underscore their complementary roles in the comprehensive analysis and preservation of wall paintings. Quantitatively, local surface roughness parameters (*Sa*, *Sq*) were found to correlate with THz signal attenuation. Topography-induced false positives were eliminated by correlating with surface morphology. Meanwhile, geometric reconstruction errors for the detected subsurface motifs remained within approximately 20 % across techniques.

Section: RESEARCH PAPER

Keywords: active thermography; THz imaging; 3D microprofilometry; fresco painting; surface and subsurface analysis

Citation: E. Vannini, I. Catapano, A. Dal Fovo, V. di Sarno, A. Rocco, P. Maddaloni, R. Fontana, Visible-to-terahertz integrated 2D and 3D imaging of surface and subsurface features in a fresco mock-up, Acta IMEKO, vol. 15 (2026) no. 4, pp. 1-10. DOI: 10.21014/actaimeko.v15i4.2393

Section Editor: Fabio Leccese, Università Degli Studi Roma Tre, Rome, Italy

Received April 30, 2026; **In final form** November 24, 2026; **Published** December 2026

Copyright: This is an open-access article distributed under the terms of the Creative Commons Attribution 4.0 International License.

Funding: This work was supported by PNRR CHANGES (Cultural Heritage Active In-novation for Sustainable Society) Project (PE_00000020), CUP_D53C22002560006, funded by the European Union—Next Generation EU M4.C2.1.3, PNRR H2IOSC (Humanities and Cultural Heritage ItalianOpen Science Cloud) Project (IR0000029), CUP_B63C22000730005, funded by Next Generation EU, PRIN-PNRR AIPAD (Artificial Intelligence and Physics for Art Diagnostics) Project (P2022SFEPN), CUP_B53D23029240001, funded by the European Union – Next Generation EU M4.C2.1.1., and project SHINE, Strengthening the Italian Nodes of E-RIHS, Avviso 424/2018 Azione II.1 PON R&I 2014–2020, DD 461 14/03/2019, PIR01-00016, CUP B27E19000030007.

Corresponding author: Emma Vannini, e-mail: emma.vannini@ino.cnr.it

1. INTRODUCTION

The structure of a mural painting varies significantly depending on the artistic technique employed. Traditional murals typically feature a complex, multi-layered stratigraphy of plaster (slaked lime mixed with sand of varying grain sizes). This sequence begins with the *arriccio* (coarse plaster) and concludes with the fine *intonachino* (fine and smoothed plaster), each prepared with progressively finer sand to achieve a smooth surface suitable for pigment application.

Owing to this complex, multilayered structure, wall paintings are prone to deterioration that affects both surface and subsurface strata. Common degradation phenomena, often caused by fluctuations in temperature and relative humidity, include detachment of the paint layer, efflorescence resulting from salt crystallization, and the formation of micro-fractures. In

deeper layers, structural defects such as air gaps and cracks frequently emerge. Furthermore, historical murals sometimes conceal earlier artworks beneath layers of white or pigmented slaked lime, applied either during restoration or to prepare a new painting surface.

The penetration capabilities of infrared radiation make Near-Infrared (NIR) reflectography and active thermography in the Mid-Wave (MWIR) and Long-Wave Infrared (LWIR) ranges effective non-invasive methods for investigating subsurface features in mural paintings [1]–[5]. For example, in [6], the authors successfully reconstructed the internal detachments of Leonardo's *Monocromo* using an innovative dual-mode approach. Furthermore, thermography has recently been used to characterize material alterations in archaeological finds by assessing emissivity changes [7], [8]. Other contemporary studies have focused on thermal IR analysis of hypogeal wall paintings to correlate temperature and humidity fluctuations with subsurface anomalies and zones of weakened adhesion [9], [10].

Over the last decades, reflection-mode Terahertz (THz) imaging has also demonstrated considerable potential in the analysis of wall paintings. Its ability to reveal hidden features with high sensitivity has further established its value within the field of cultural heritage diagnostics [11]–[15]. Moreover, recent advances in THz radar technology have shown its capability to detect millimetre-scale cracks in ancient mural structures [16].

When these techniques are employed for the diagnosis of defects in mural paintings, the effect of surface morphology must be taken into account. Surface irregularities, such as crack patterns, morphological discontinuities, material inhomogeneities and detachments, can significantly affect the recorded signal in both the THz and IR ranges [17], [18]. The coarse and irregular granularity of a covering plaster may induce signal scattering, thereby reducing the detectability of subsurface features or generating artifacts arising from surface irregularities. In reflection-based measurements, rough surfaces are known to cause a more significant reduction in reflectivity at normal incidence compared to smooth surfaces [19]. This effect can be exploited for collecting micromorphological data on the surfaces under study. To this end, the main challenge is to correlate the THz-reflected pulses to the surface texture parameters. Cacciari et al. [20], [21] report one of the first applications of THz time domain spectrometry (TDS) to estimate the roughness parameters of both outer and inner interfaces of a material layer. The results achieved were congruent with the corresponding *Rq* parameter measured using contact profilometry and 3D microscopy. While the cited studies were limited to corroded metal surfaces, other works report the geometrical surface reconstruction through THz spectroscopy on fresco samples [18]. Therefore, the 3D reconstruction of the surface morphology and its characterization through specific parameters are valuable tools for qualitatively and quantitatively assessing the effect of topography on reflection-based measurements of irregular surfaces. Laser scanning microprofilometry is an effective technique for high-resolution surface 3D modelling. This technology can be applied to a variety of artistic materials and has proven effective in mapping the surface morphologies with high resolution [22], [23].

This study presents a diagnostic protocol designed to evaluate the effectiveness of Infrared and Terahertz radiations in detecting concealed features within mural paintings, and to assess their individual and combined potential. To this purpose, a mock-up was prepared following traditional *buon fresco* stratigraphy and incorporating hidden decorations. It was fabricated featuring irregular, low reflective surfaces, such as plaster, combined with high-reflectivity materials, including gold and silver, used to replicate metallic decorations. The technological suite comprised four instruments: a multi-spectral scanner operating in the Vis-NIR range (395–2550 nm), two thermal cameras covering the mid (3–5 μm) and long-wave (8–14 μm) IR ranges, and a THz spectrometer. An optical scanning microprofilometer, custom-developed at CNR-INO, was also employed to acquire accurate 3D models of the surface topography. The use of such transportable instrumentation enables the eventual replication of this multi-technique approach on real mural paintings under vertical and uncontrolled environmental conditions. Although the use of microprofilometry on real wall is restricted to a very limited number of case studies, the feasibility of surveying difficult-to-reach surfaces has been demonstrated, establishing it as a valuable technique for use on scaffolding or in challenging operational contexts [24], [25].

This work further aims to investigate the discrimination and mitigation of artefacts arising from surface morphology. As previously reported, the effect of topography on both IR and THz signals has already been investigated; however, in this paper, the separation of long- and short-wavelength surface components (waviness and roughness, respectively) and the computation of local surface roughness parameters (*Sa* and *Sq*) [26], [27] have been applied to effectively and quantitively detect artifacts and false-positive features in IR and, more notably, in THz signals. To the best of our knowledge, this is the first investigation into how surface wavelength components affect THz signals on mural-painted surfaces made from either plaster or lime-wash.

In conclusion, this study not only demonstrates the suitability of an integrated, multi-technique approach for in situ application—pending further validation on authentic mural paintings—but also proposes a new pipeline for the quantitative resolution of artifacts caused by surface irregularities, typically too fine and detailed to be detected by the naked eye.

The article is structured into five sections. The first section is the introduction. Section 2 describes the fresco mock-up preparation, while Section 3 outlines the instrumentation, acquisition parameters, experimental setups, and data processing. The results are presented and discussed in Section 4. Finally, Section 5 concludes the paper with a summary of the main achievements and findings.

2. MATERIALS

The analysed sample was professionally prepared by the art conservator Ezio Buzzegoli to simulate the stratigraphy of mural paintings and replicate decorative elements concealed due to past restorations or repainting purposes. The object consists of a terracotta slab (35×45 cm^2) divided into nine sections (7×11 cm^2 each, numbered from 1 to 9), arranged in three rows (Figure 1a). Fabricated using the traditional fresco technique, the mock-up preparation employed materials, including plaster, pigments, and metals, selected according to historical recipes and traditional execution protocols derived from ancient master painters.

Each section features an *arriccio* base layer (~2–3 mm thick) composed of slaked lime (calcium hydroxide) and coarse sand in a 1:2 ratio. The coarse aggregate consisted of a dried silica sand (SiO_2 ~ 70 %, Fe_2O_3 < 4 %, CaO < 10 %) with a granulometry ranging from 0.4 to 1.4 mm and a grain fineness number of 20–

25. The slaked lime employed was an air-setting binder composed of calcium hydroxide and water. Some preparatory drawings were applied on top of the *arriccio*. These were executed in iron oxide and carbon black, which were the materials most used for design transfer. They are fully visible in area 1 (top left corner of the slab).

From areas 2 to 9, a painted fine plaster layer called *intonachino* (slaked lime and fine sand in a 1:2 ratio), visible in area 2, was applied over the *arriccio*. This layer has a thickness of 1.5–2 mm. The fine aggregate consisted of a dried silica sand (SiO_2 ~ 70 %, Fe_2O_3 < 4 %, CaO < 10 %) with a granulometry ranging from 0.1 to 0.45 mm and a grain fineness number of 40–50.

Owing to their distinct aggregate compositions, the *arriccio* and *intonachino* layers differ in granulometry. The irregular and coarse sand of the *arriccio* yields higher porosity, whereas the *intonachino* is characterized by a considerably smoother and more regular surface. The mixture of slaked lime and sand contained no additional performance-enhancing materials, such as *pozzolana* (a volcanic ash) or marble dust, and only water was added.

The pigments used were traditional wall painting pigments (Verona green earth for green, red ochre and *lacca di garanza* for red, and ultramarine blue and natural indigo for blue). Area 3 simulates the application of decorative elements in gold and silver leaf over the painted surface. These were applied via the mordant (oil) gilding technique, an effective method for applying metal leaf on mural paintings. In the past, these kinds of decorations were applied for embellishments or haloes.

The second row replicates the historical practice of overpainting, where a new plaster layer was applied over an existing work. This overlying layer was left unpainted in area 4, painted in area 5, and decorated with metallic leaf in area 6.

The third row examines *scialbatura*, a technique used to conceal underlying paintings with a thin lime wash layer (thickness of a few hundred μm). *Scialbo* consists of a mixture of lime wash, starch tempera, and fine-grained pigments. In this work, it was applied in white (area 7), yellow (area 8), and green (area 9) to replicate some of the most prevalent varieties of *scialbatura* encountered in fresco paintings.

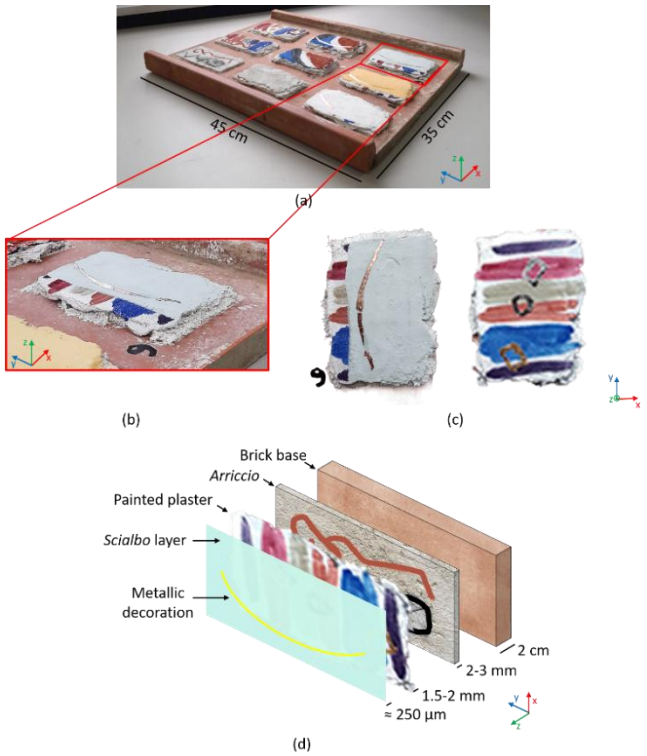


Figure 1. (a) Fresco mock-up; area 9; (b) detailed magnification; (c) visible surface (left) and photograph captured during sample preparation, showing the subsurface painted area (right); (d) schematic cross-sectional representation.

Each area incorporates the treatments from the previous ones. Area 9, located in the lower right quadrant of the terracotta slab (Figure 1b to Figure 1d), represents a complete and realistic stratigraphic profile. This is why the focus of this study is on this area. The stratigraphy of this region, exemplified in Figure 1d, consists of an underlying painted layer featuring three gold and silver leaf decorations, overlaid by a thin green *scialbo* layer. The three metallic decorations are positioned at the centre of the surface, arranged vertically from top to bottom. The upper two decorations are made of silver, while the lowest is gold. This gold decoration is located beneath a visible, arc-shaped metallic decoration on the surface. The top and bottom features form the contours of a rectangular shape (approximately 1 × 1.5–2 cm²), whereas the central feature is circular, with a diameter of approximately 1.5 cm. Since these elements are located beneath the *scialbo* layer, they lie at a depth of a few hundred micrometres. The width of the gold and silver lines ranges from 2.5 to 4.5 mm; this irregularity is attributable to the mock-up's manual execution.

Finally, several months were allowed to elapse between sample preparation and testing, to ensure that the carbonation (curing) was substantially complete.

3. METHODS

3.1. Vis-NIR Reflectance Imaging Spectroscopy (RIS)

The visible and near-infrared spectral ranges were investigated using a multispectral scanner developed by the Heritage Science group at CNR-INO, Florence (Figure 2a) [28]–[30]. The device performs non-contact reflectance measurements, integrating whiskbroom scanning with pointwise spectral information acquired across the 395 nm to 2550 nm range.

The scanning unit comprises a mechanical movement system that displaces both the illumination and detection assemblies. A 45°/0° illumination/detection geometry was adopted in accordance with the guidelines of the Commission Internationale de l'Éclairage (CIE) for non-contact reflectance measurements. The illumination system consists of two low-voltage halogen lamps and two white LEDs, illuminating an area of a few centimetres in diameter. The detection system employs a catoptric lens composed of two opposing parabolic mirrors, which produce aberration-free images with a 1:1 magnification ratio. The lens collects backscattered radiation from the object and focuses it onto a bundle of 36 optical fibres arranged in a square configuration (six fibres per side), which transmit the radiation to the detection system. The latter comprises a set of silicon (Si, 395–950 nm) and indium gallium arsenide (InGaAs, 1050–2550 nm) photodiodes, each coupled with an interferential filter for wavelength selection.

The spectral resolution ranges from 20 to 30 nm in the visible region, and from 66 to 120 nm in the near-infrared region. The instrument is equipped with an autofocus system consisting of a laser distance meter based on the triangulation principle, which maintains the correct working distance during scanning.

The system can acquire a maximum area of 1 m² in approximately 3 hours, with a sampling step of 250 μm (4 pixels/mm) and a scanning speed of 500 mm/s.

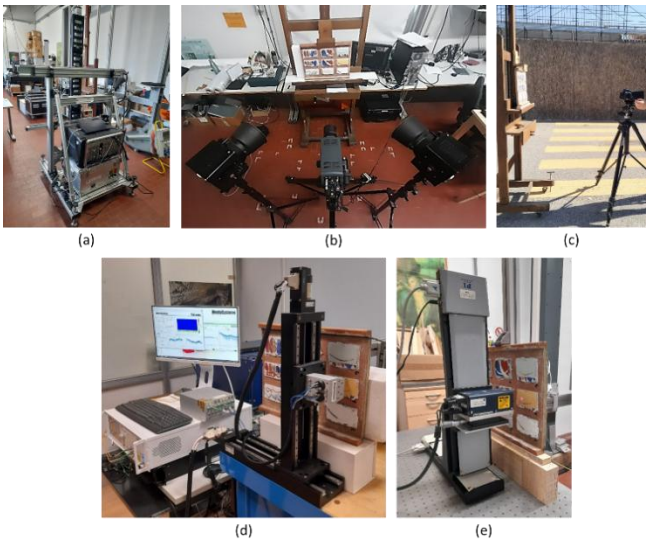


Figure 2. (a) Vis-NIR multispectral scanner developed at CNR-INO; indoor thermographic survey in the 3–5 µm range (b) and outdoor thermographic survey in the 8–14 µm (c) range; (d) THz measurement performed at CNR-IREA; (e) 3D microprofilometry analysis conducted in the laboratory of CNR-INO, Florence.

The output consists of a set of 32 co-registered monochromatic images: 16 in the visible region and 16 in the near-infrared region [31]. These images form the RIS data cube, and are perfectly superimposed and metrically accurate. These data enable both single-wavelength image analysis and spectral profiling at user-defined points.

The fresco mock-up was scanned in a single acquisition covering an area of 26.7 × 41.7 cm².

3.2. MWIR active thermography

Mid-wave infrared analysis was performed using a FLIR A6751 MWIR thermal camera equipped with an indium antimonide (InSb) detector sensitive in the 3–5 µm range. The detector features a 640 × 512 pixel array with a 15 µm pitch, and achieves a Noise Equivalent Temperature Difference (NETD) < 20 mK, with an accuracy of ± 2 °C. The camera operates within an ambient temperature range of –40 °C to 50 °C and a measurement range of –20 °C to 350 °C, at frame rates of up to 480 fps. The thermal camera was equipped with a 17 mm lens with f/2.5. Acquisition was controlled using the ResearchIR MAX proprietary software.

The thermographic analysis was conducted inside the CNR-INO laboratory (Figure 2b) under controlled environmental conditions, with the ambient temperature held at (20 ± 1) °C and relative humidity of (50 ± 5) % maintained constant throughout the acquisition session. Two 1000 W halogen lamps were symmetrically positioned approximately 100 cm from the terracotta sample for uniform illumination of the area within the camera's field of view (FOV). The camera-to-object distance was set to approximately 90 cm to set up an acquisition geometry to achieve sub-millimetric spatial resolution (~ 0.8 mm). The heating protocol consisted of a continuous thermal stimulation lasting 3 s to detect small features under thin films. Immediately after the heating phase, the lamps were removed from the recording area to avoid the residual emission from the halogen bulbs, which lies in the MWIR region and would otherwise have dominated the recorded signal. The thermal data sequence was obtained by recording both the heating and cooling phases at a rate of one frame per second (1 fps). The cooling process was recorded until thermal equilibrium between the sample and the external environment was reached. Only the thermal relaxation was investigated, as the reflected lamp signal had a strong influence on the radiation detected during the heating phase. Emissivity was not measured directly on the sample, but was set to 0.9, which is the characteristic emissivity of mortar or plaster. The resulting thermal data cube consists of N time-resolved thermal images (N being the cooling duration as expressed in seconds), which can be analysed as individual frames or as temperature profiles. The videos, exported as TIFF stacks, were processed in the MATLAB® environment.

3.3. LWIR active thermography

Long-wave infrared measurements were performed using a TESTO 890 thermal camera equipped with an uncooled microbolometer detector sensitive in the 8–14 µm range. The camera features a resolution of 1280 × 960 pixels, a NETD of < 40 mK at 30 °C, and an accuracy of ± 2 °C. The camera has an operational range of –15 °C to 50 °C, and a measurement range from –30 °C to 100 °C. Thermal frames can be acquired in snapshot mode directly with the camera, while data visualization and processing are performed using the Testo IRSoft proprietary software.

Since long-wave infrared (LWIR) thermography performed indoors with halogen lamps failed to detect any subsurface features, measurements were taken outside on a sunny day in September 2025, exploiting solar radiation as the heat source (Figure 2c). During the outdoor session, the ambient temperature was approximately 24 °C, with stable solar irradiance and negligible wind interference to minimize thermal drift. Thermal images were captured with an emissivity value of 0.9.

3.4. THz Time-Domain Imaging

THz analysis was performed at CNR-IREA using a Menlo Systems TeraASOPS spectrometer (Figure 2d), based on the Asynchronous Optical Sampling (ASOPS) principle [32]. The system can be configured to acquire data in either transmission or normal reflection mode. It has a nominal bandwidth (B) of 4 THz and a reference signal-to-noise ratio greater than 70 dB, which are achievable under operational conditions of 10 Hz laser difference frequency, 10 MHz sampling rate, 10^6 gain, 1000 waveform averages, and favourable environmental conditions [33]. Accordingly, in the case of normal reflection measurements, the maximum investigated depth ($z_{\max}$) is defined by equation (1):

$$z_{\max} = \frac{T_{\max} \cdot v}{2}, \tag{1}$$

where v is the electromagnetic wave propagation velocity in the encountered materials and $T_{\max}$ is the system's maximum observation time window of 100 ps, which is movable across a 10 ns range. Note that $z_{\max}$ is always less than 1.5 cm. This upper bound corresponds to propagation in air (i.e. $v \approx c = 3 \times 10^8\, m/s$); for propagation within a material of refractive index n ($v = c/n < c$), $z_{\max}$ is correspondingly smaller. However, in this study, the practical penetration limit was confined to a few hundred microns (equivalent to the thickness of the *scialbo* layer) and did not successfully penetrate the *intonachino* thickness (1.5–2 mm).

The depth resolution is defined by equation (2):

$$\Delta_z = \frac{v}{2\,B}, \tag{2}$$

where B is the bandwidth. When normal reflection data are gathered in uncontrolled conditions, the frequency range is reduced to about 2 THz. Hence, the expected range resolution is approximately 100 μm in air.

The system is equipped with a motorised xy scanner, enabling the THz probe to move automatically across the surface of the object under examination. The maximum scanning area is 30 × 30 cm², with a minimum spatial step of 100 μm.

THz images were acquired over area 9 with a spatial step of 0.5 mm. The laboratory environment was maintained at a stable temperature of 21 °C, with relative humidity below 45 %, to minimize water vapor attenuation along the THz beam path.

To minimize the impact of measurement and environment noise and to account for time-delay variations caused by irregular surface topography, the time-domain THz waveforms were processed using the chain detailed in [34], [35]. Two-dimensional THz images were generated by mapping the peak maximum, peak minimum, or total energy of the time-domain waveforms at each pixel. These 2D reflectivity maps allow for the detection of materials with different refractive indices, but they lack depth information and are therefore unsuitable for stratigraphic characterization. To resolve the internal structure and identify potential subsurface layers, radargrams (also referred to as B-scans or cross-sectional images) were generated along both the x and y directions [36].

3.5. Optical microprofilometry

High-resolution 3D models of the sample surface were generated using an optical microprofilometer developed at CNR-INO (Figure 2e). The device consists of a commercial probe mounted on an xy scanning system (scanning precision: 0.1 μm; maximum scanning area: 30 × 30 cm²). The scanning speed ranges from 100 to 400 points/s depending on the sampling step and the travel length. The probe can be equipped with lenses of various focal lengths. Since the measured surfaces were nearly flat, a 50 mm lens was selected, providing a spot diameter of 37 μm at the beam waist and a working distance of 44 mm, with a dynamic range of 8 mm. To balance acquisition time and scanning quality, the three rows were acquired separately with a spatial offset of 50 μm.

The system outputs high-resolution topographic maps, which can be exported as either 3D models or high-fidelity 2D images. To ensure spatial accuracy, we processed the 3D data in MATLAB® environment by subtracting a first-order best-fitting plane. This effectively eliminates any deformation caused by probe-to-object misalignment during the scan. To quantitatively evaluate the impact of optical microprofilometry on data interpretation, the 3D datasets were filtered to isolate surface roughness from waviness through the selection of an appropriate spatial wavelength. Whereas roughness is attributable to the material's microstructure, waviness reflects broader surface deviations. Since a fixed spatial threshold for distinguishing between these two components is not established in cultural heritage applications, the optimal wavelength cut-off (λc) was determined through a series of qualitative visual assessments. Starting from the first order fitted surface, which encompasses both short-wavelength (roughness) and long-wavelength (waviness) features, a phase-correct Gaussian filter was applied. Subsequently, the local surface roughness parameters (namely, the arithmetic mean height (Sa) and the root-mean-square height (Sq) [26]) were computed on four selected ROIs within area 9.

Additionally, we enhanced surface legibility by generating digital grazing-light images. Using specialized embossing filters, we simulated specific light directions on the models, revealing fine surface details that often surpass the clarity of traditional photography.

3.6. Data co-registration and comparative analysis

To ensure cross-dataset consistency and enable an effective multi-analytical assessment, spatial co-registration and comparative interpretation were performed. Given the different spatial resolutions of the instruments employed, pixel-level data fusion was not pursued. Instead, the 2D images extracted from the IR and THz-TDI datasets were spatially aligned using prominent structural landmarks of the mock-up (e.g. the visible margins of Area 9 and the surface metallic arc) as geometric control points. The high-resolution topographic map acquired via optical microprofilometry served as the spatial reference framework. This approach facilitated a direct, layer-by-layer comparative interpretation, enabling cross-validation of subsurface feature detection while minimizing artifacts attributable to surface roughness.

4. RESULTS

Neither technique successfully revealed the painted or gilded elements concealed beneath the plaster stratum (the second row of the mock-up). This limitation was likely attributable to two principal factors: the thickness of the overlying layer, which attenuated the probing signal, and the coarse, irregular granularity of the plaster, which induced significant signal scattering. By contrast, metallic decorations located beneath the *scialbo* layer were successfully detected, thanks to the layer's small thickness and fine, uniform grain structure. In the following, the attention is focused on the most significant results obtained by applying the cited techniques, whose technical specifications are summarized in Table 1. Specifically, this section presents results referred to area 9.

This section is divided into two parts. Subsection 4.1 relates to the detection of subsurface features across different spectral

Table 1. Technical specifications of the analytical techniques employed in the present study.

Technique	Spectral range	Spatial resolution	Max Penetration Depth	Acquisition time	Signal-to-noise ratio
Vis-NIR Reflectance Imaging Spectroscopy	395–2550 nm	250 μm	Depends on the material	3 h for 1 m²	NA
MWIR Active Thermography	3–5 μm	≈ 0.8 mm	Depends on the material	Set by the user	NETD < 20 mK
LWIR Active Thermography	8–14 μm	≈ 0.9 mm	Depends on the material	Set by the user	NETD < 40 mK
THz Time Domain Imaging	75–3000 μm	0.5 mm	Depends on the material (< 1.5 cm for the adopted system)	1 h for 100 cm²	70 dB
Optical microprofilometry	≈ 635 nm	50 μm	No depth information	Scanning speed from 100 to 400 points/s	Negligible noise

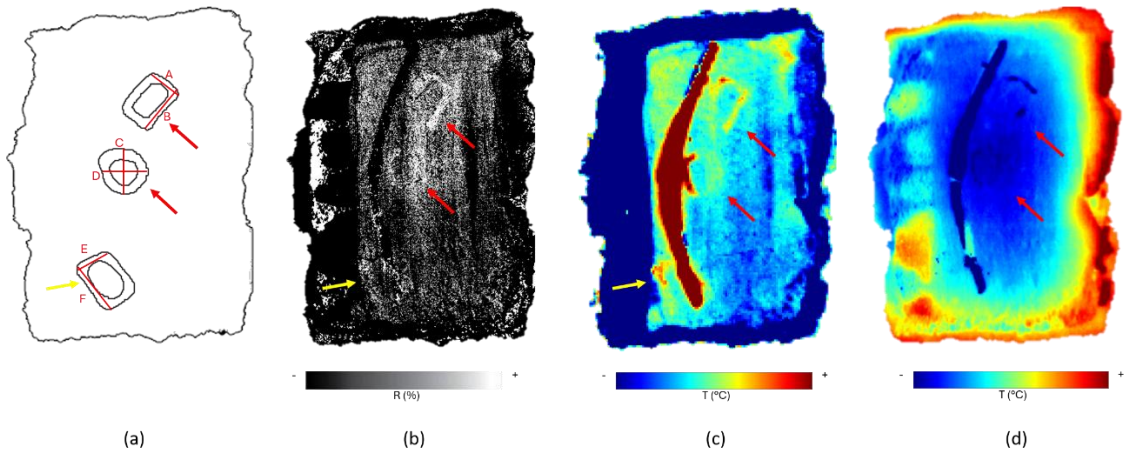


Figure 3. (a) Schematic representation of the geometric shapes comprising the underlying layer. Red lines (A–F) indicate the dimensions measured for geometric error quantification. (b) Reflectance image acquired at 1050 nm; thermal images in the 3–5 µm (c) and 8–14 µm (d) spectral bands. Red arrows denote the two uppermost decorative elements, whereas yellow arrows indicate the lowermost decoration, which is detectable in (c) and faintly visible in (b) (see Figure 1c for reference).

ranges. Subsection 4.2 relates to the correlation of signal anomalies with surface microtopography.

4.1. Subsurface metallic decoration detection

Some variations emerged in the techniques' detection capabilities regarding both the number of detected decorations and the geometric precision of their outlines (see Figure 3b–d for results in the infrared range).

The spatial sampling step varied among the techniques, ranging from 250 µm for the VIS–NIR scanner to 50 µm for the microprofilometer, while THz measurements were acquired with a 500 µm step. This allowed us to successfully detect the smallest metallic features having an approximate diameter of about 4 mm.

LWIR thermography resolved only two of the three metallic elements, whereas NIR reflectography, MWIR thermography, and THz imaging confirmed the presence of the third, lower-positioned decoration (yellow arrows in Figure 3 and Figure 4b). This detection discrepancy may arise from either the obscuring effect of overlying gold leaf or morphological irregularities at the surface.

Among the modalities tested, THz imaging proved the most effective, providing a complete reconstruction of all metallic motifs. Furthermore, the radargrams (Figure 4c and Figure 4d) successfully localized the metallic features within the subsurface layers, confirming their depth and stratigraphic position.

Differences in thermographic surveys arose from the spectral ranges investigated. In the MWIR range (3–5 µm), the ability to identify metal decorations was primarily driven by the high reflectivity of the metal, rather than its thermal emission, owing to the material's extremely low emissivity. In contrast, LWIR imaging (8–14 µm range) under solar radiation identified metal leaves through thermal contrast. The slow, diffuse nature of solar heating allowed a sufficient thermal gradient to develop between the limewash and the underlying metal.

Further observed differences concerned the central metallic motif, whose representation varied across techniques. While some modalities highlighted only the left portion (Figure 3b), others emphasized the right sector (Figure 4b). Such variations are attributable to variations in surface microtopography (see Subsection 4.2).

The detection rate and geometric error of each technique were quantified by measuring the dimensions of the detected shapes. Using the reference measurements obtained from the underlying layer, the percentage deviation of the dimensions reconstructed by each method was calculated. The results summarised in Table 2 confirm the superior performance of THz imaging and MWIR thermography. The THz errors of -15 ± 2 % and 19 ± 4 % for dimension D and E are outliers compared to other THz values (all ≤ 10 % in magnitude). This is likely due to the arc-shaped metallic decoration on the surface, which greatly reduces the detectability of the motifs.

4.2. Correlation of surface microtopography with imaging results

As noted in Section 4.1, several observations from the MWIR and THz surveys were more closely associated with surface microtopography than with subsurface stratigraphic discontinuities or pigment distribution.

To investigate this further, we analysed high-resolution 3D models of the surface morphology generated via optical microprofilometry. By varying the direction of the simulated grazing light in the processed images, we successfully mapped all topographic surface features.

The results are summarized in Figure 5. Of note are the anomalous signals identified in the THz normalized minimum map (Figure 5a), which correspond directly to the surface irregularities marked by the white arrows in the figure.

The discrepancies observed when reconstructing the circular shape of the central decoration are also attributable to surface morphology. As illustrated in Figure 5d, a vertical line bisects the feature. This line is clearly identifiable in the MWIR thermal image but remains indistinguishable in the LWIR range, where no difference is observed between the left and right sections of the decoration. This variation further confirms that surface

Table 2. Geometric error associated with defect detection. Letters A–F denote the geometric features labelled in Figure **3**a.

	Theoretical value	NIR	MWIR	LWIR	THz
A	1.11 ± 0.02 cm	-6 ± 3 %	-4 ± 2 %	-15 ± 3 %	5 ± 6 %
B	1.59 ± 0.02 cm	-5 ± 3 %	-6 ± 1 %	-34 ± 1 %	-3 ± 2 %
C	1.46 ± 0.05 cm	-11 ± 3 %	7 ± 3 %	-13 ± 5 %	1 ± 5 %
D	1.50 ± 0.02 cm	-29 ± 2 %	-8 ± 2 %	-38 ± 1 %	-15 ± 2 %
E	1.12 ± 0.04 cm	-24 ± 4 %	10 ± 4 %	Not detected	19 ± 4 %
F	1.74 ± 0.02 cm	-16 ± 2 %	-8 ± 11%	Not detected	3 ± 2 %

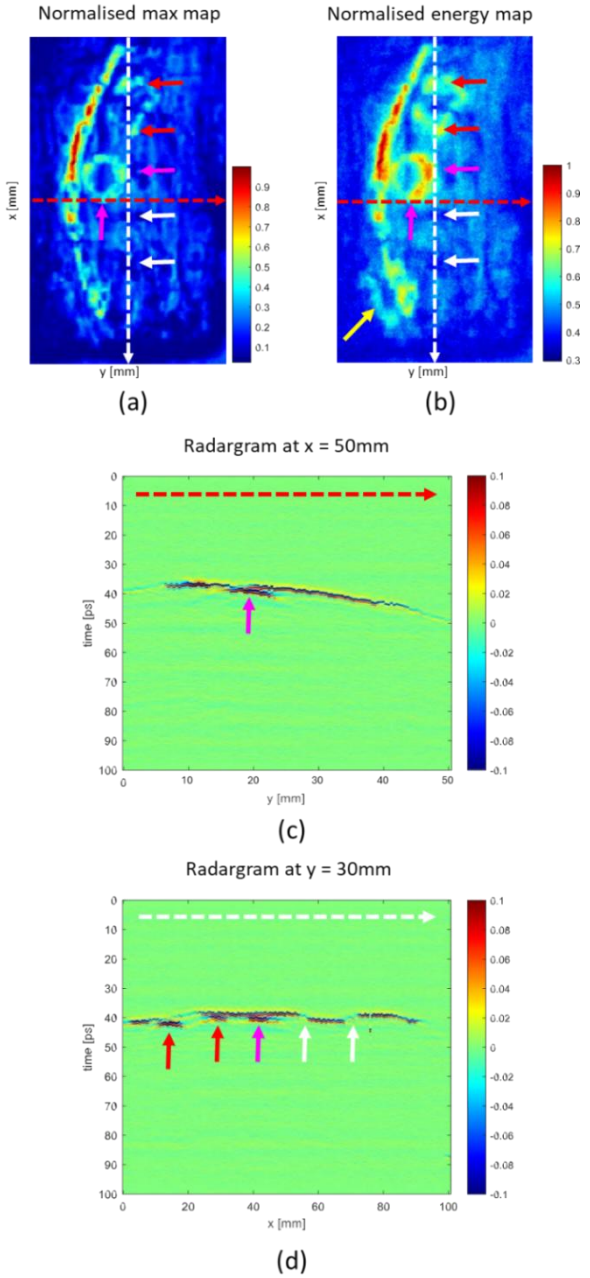


Figure 4. THz imaging results: normalised [0–1] maximum (a) and total energy (b) reflectivity maps of the THz signal. Horizontal (red) and vertical (white) dotted arrows indicate where the radargrams shown in (c) and (d) were extracted. Red and magenta arrows indicate the two uppermost subsurface metallic decorations, whereas the yellow arrow in (b) indicates the lowermost decoration. White arrows indicate the anomalous signals possibly correlated with surface features.

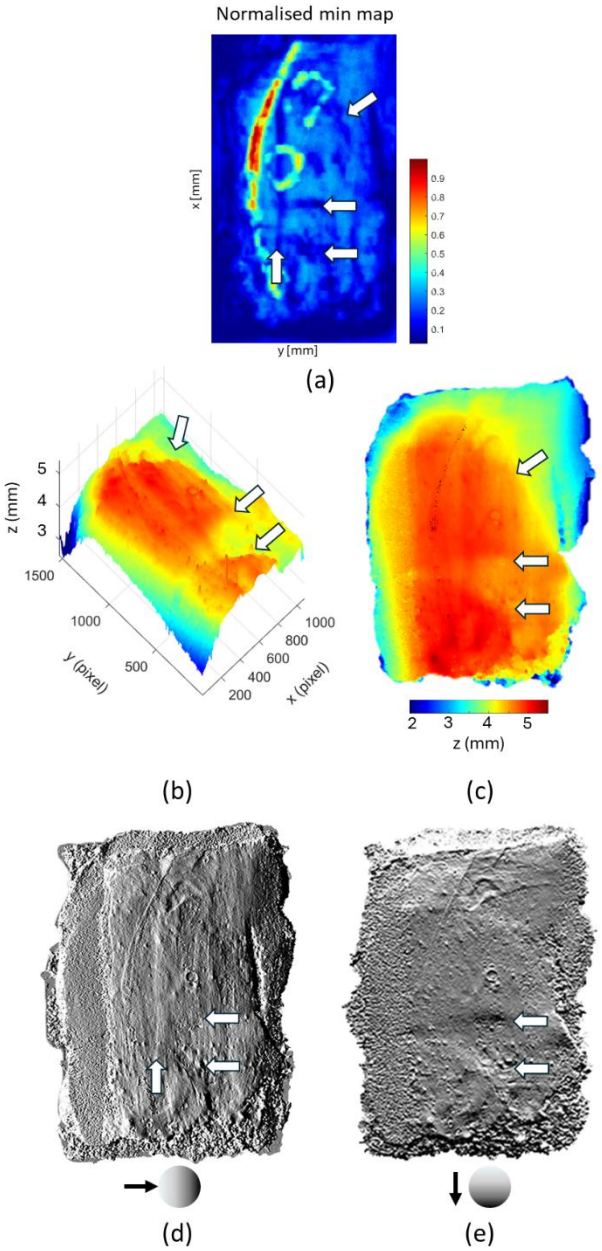


Figure 5. (a) Normalised [0–1] minimum reflectivity map of the THz signal; (b) 3D model and (c) topographic map obtained with the optical microprofilometer; (d) and (e) grazing-light images with two different incident light directions. White arrows indicate the anomalous signals correlated with surface features.

effects exert a significantly stronger influence within the MWIR spectrum, where reflection is dominant.

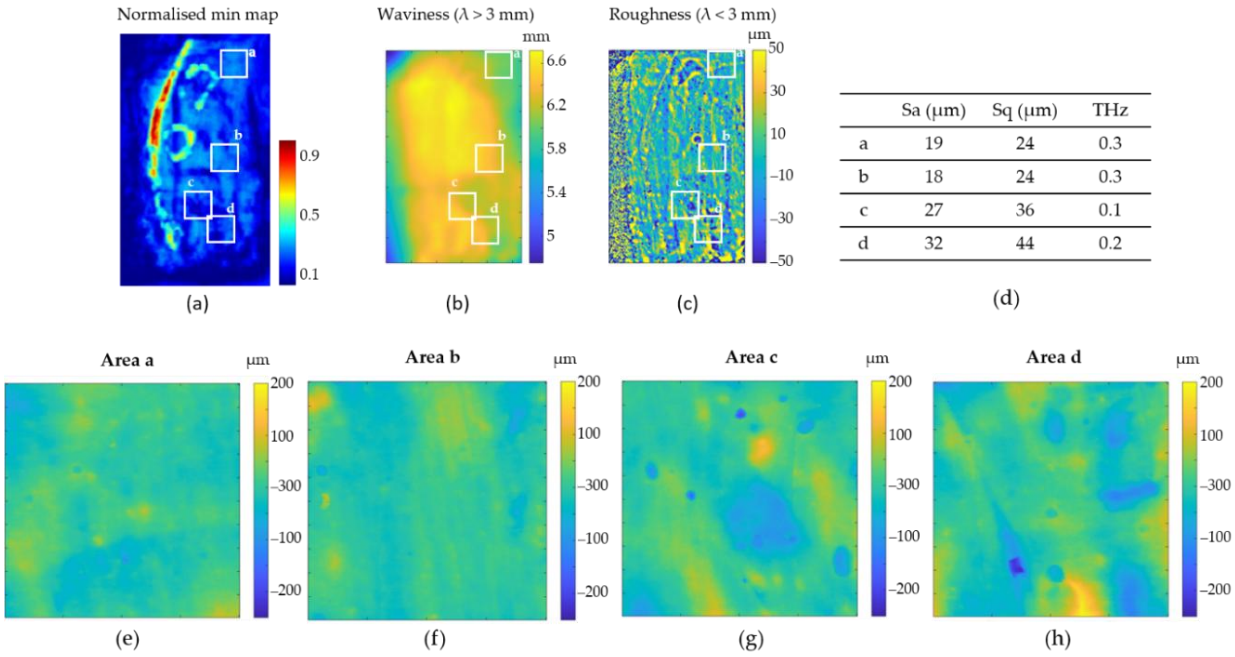
To evaluate the impact of optical microprofilometry on data interpretation, surface roughness parameters (*Sa* and *Sq*) were computed across four selected regions of interest (ROIs), as shown in Figure 6. An inverse correlation between THz reflectivity intensity and surface heterogeneities corroborated our qualitative observations. Specifically, areas c and d exhibited high *Sa* and *Sq* values, which corresponded to markedly low THz signals, whereas areas a and b displayed lower roughness values and higher THz signal intensities. A strong negative trend was observed between surface roughness (*Sa* and *Sq*) and THz signal intensity (Pearson coefficient, r = -0.73 and -0.71 for *Sa* and *Sq*, respectively). However, given the limited sample size (n = 4 ROIs, degrees of freedom = 2), this correlation is reported strictly as descriptive evidence supporting surface scattering, rather than as a statistically significant result (p-value = 0.27).

Consequently, the four false positives induced by surface irregularities (see the white arrows in Figure 4 and Figure 5) were visually eliminated by checking their spatial correlation with the superficial topography.

Distinguishing between waviness and roughness further revealed that the THz signal is influenced by both spectral components.

4.3. Measurement uncertainty and potential sources of error

In this multi-technique survey, several factors influence the measurement uncertainty and signal robustness across the different spectral ranges. The primary source of uncertainty in



	Sa (μm)	Sq (μm)	THz
a	19	24	0.3
b	18	24	0.3
c	27	36	0.1
d	32	44	0.2

Figure 6. (a) Normalized THz min map; (b) waviness map; (c) roughness map. White rectangles highlight the ROIs selected for surface calculation and named a–d. (d) Table summarizing roughness parameters and relative THz intensity; (e)-(h) fitted surfaces of the ROIs.

active thermography arises from surface emissivity variations and local reflectivity fluctuations driven by surface roughness. As discussed above, the MWIR signal is heavily dominated by surface reflection, rather than pure thermal emission, resulting in geometric distortions in the reconstruction of the central circular decoration. In the LWIR range, the diffuse nature of the heat source induces edge blurring, which reduces the detectability of fine details. The uncertainty in THz reflectivity maps is mainly attributable to the scattering caused by surface roughness, which induces localised signal attenuation. Although instrument electronic noise is effectively minimized through a high reference signal-to-noise ratio (>70 dB) and waveform averaging, the uneven topography remains a significant source of artifact. Furthermore, measurement uncertainty arises in the quantification of the detection rate and geometric error of the accuracy of detectability of each technique (see the error bars in Table 2). Conversely, the error on the *Sa* and *Sq* parameters calculation depends on the reproducibility (dynamics) of the instrument (1 μm).

5. CONCLUSIONS

This study analysed a prepared fresco mock-up designed to simulate the traditional stratigraphy of murals, in which existing paintings are covered with new layers of plaster or limewash. A multi-technique approach was employed to analyse both surface and subsurface layers using Vis-NIR multispectral reflectance spectroscopy, active thermography (in the MWIR and LWIR ranges), Terahertz Time-Domain Imaging (THz-TDI), and optical microprofilometry for topographic reconstruction. Table 3 summarises the performance of these techniques.

The results confirmed the complementary diagnostic capabilities of the investigated modalities. Metallic decorations located beneath a thin *scialbo* layer were detected by most techniques, although with different levels of sensitivity and geometric accuracy. Among them, MWIR thermography and THz imaging provided the most reliable reconstruction of the concealed motifs (see Table 2). The latter also enabled their stratigraphic localization through radargram analysis. In contrast, LWIR thermography showed lower sensitivity to the smallest decoration, while NIR reflectography allowed partial identification of the hidden elements.

The differences in thermographic performance were likely attributable to distinct physical mechanisms. MWIR imaging was heavily influenced by surface morphology due to the dominance of reflected signals. In contrast, LWIR imaging relied on thermal contrast generated by diffuse, gradual heating from solar radiation and was therefore less affected by surface topography.

As reported in Table 3, under the specific experimental conditions of this fresco mock-up, the practical penetration limit for all investigated optical and thermal ranges is confined to a few hundred microns (corresponding to the thickness of the

Table 3. Performances of the analytical techniques employed in the present study.

Technique	Detection depths limits	Main diagnostic capability	Main limitation
Vis-NIR Reflectance Imaging Spectroscopy	A few hundred microns	Detection of shallow subsurface features and pigment contrast	Limited penetration depth
MWIR Active Thermography	A few hundred microns	Detection of reflective metallic features beneath thin layers	Strong influence of surface reflectivity
LWIR Active Thermography	A few hundred microns	Detection based on thermal contrast	Lower sensitivity to small features
THz Time Domain Imaging	A few hundred microns	Reconstruction of subsurface metallic decorations and stratigraphy	Signal affected by surface roughness
Optical microprofilometry	No depth information	High-resolution surface topography reconstruction	Surface information only

scialbo layer). None of the techniques successfully penetrate the thickness (1.5–2 mm) and low optical contrast of the fine plaster layer.

A key outcome concerns the influence of surface morphology on the measured signals. The comparison between THz reflectivity maps and MWIR thermal images with microtopographic models revealed that several anomalies observed in the THz and MWIR data were associated with surface irregularities, rather than subsurface structures. These results highlight the need to account for surface roughness effects when interpreting infrared and terahertz diagnostic data.

The validation of the proposed techniques was limited to a laboratory sample. Mock-ups serve as essential simplified models for initial testing; however, they cannot fully replicate the high complexity of real-world mural paintings. These often exhibit uneven aging (resulting in heterogeneous material properties and non-uniform thermal behaviour), surface contamination (such as dust, salt crystallizations, or biological growth, which may significantly alter the optical and thermal responses of the surface), environmental fluctuations (variations in temperature, humidity, and solar irradiance, which can affect the stability and reproducibility of measurements), and intricate multi-layered stratigraphies. Therefore, future work must validate this methodology in situ, encompassing traditional *buon fresco*, *secco* paintings, and contemporary street art with varied materials and inclusions. All instruments are transportable and can be operated on scaffolding to investigate vertical painted surfaces. For indoor applications of long-wave infrared (8–14 μm) thermography, where solar radiation is unavailable, alternative diffuse thermal sources, such as portable forced-air heaters or infrared panels, can be effectively employed to overcome ambient constraints.

Overall, the study demonstrates that integrating complementary imaging techniques with high-resolution surface topography measurements improves the reliability of subsurface investigations in mural paintings and related cultural heritage artefacts.

AUTHORS' CONTRIBUTION

Conceptualization, E. V., A. D. F., and R. F.; Data curation, E. V. and I. C.; Formal analysis, E. V. and I. C.; Funding acquisition, R. F. and P. M.; Investigation, E. V., V. D. S, A. R., and I. C.; Methodology, E. V., A. D. F., V. D. S, and A. R.; Supervision, R. F.; Validation, I. C., A. D. F., R. F., V. D. S, and A. R.; Visualization, E. V. and I. C.; Writing – original draft, E. V.; Writing – review and editing, I. C., A. D. F., V. D. S, A. R., P. M., and R. F.

ACKNOWLEDGEMENT

This research was funded by the project PNRR CHANGES (Cultural Heritage Active Innovation for Sustainable Society) Project (PE_00000020), CUP_D53C22002560006, funded by the European Union – Next Generation EU M4.C2.1.1, PNRR H2IOSC (Humanities and Cultural Heritage Italian Open Science Cloud) Project (IR0000029), CUP_B63C22000730005, funded by Next Generation EU, PRIN-PNRR AIPAD (Artificial Intelligence and Physics for Art Diagnostics) Project (P2022SFEPN), CUP_B53D23029240001, funded by the European Union – Next Generation EU M4.C2.1.1., and the project SHINE, Strengthening the Italian Nodes of E-RIHS, Avviso 424/2018 Azione II.1 PON R&I 2014–2020, DD 461 14/03/2019, PIR01-00016, CUP B27E19000030007.

We gratefully acknowledge the contribution of art conservator Ezio Buzzegoli in preparing the mock-up analysed in this research.

REFERENCES

[1] J. Striova, L. Pezzati, E. Pampaloni, R. Fontana, Synchronized Hardware-Registered VIS-NIR Imaging Spectroscopy and 3D Sensing on a Fresco by Botticelli, Sensors 21 (2021) 4, pp. 1–14. DOI: 10.3390/s21041287

[2] S. Ceccarelli, N. Orazi, F. Mercuri, U. Zammit, S. Paoloni, Mid-wave infrared analysis of the wall drawing "Saint Joseph with the Child" by Gian Lorenzo Bernini, In Advanced Technologies for Cultural Heritage Monitoring and Conservation. S. Ceccarelli, M. Missori, R. Fantoni (editors). Springer, Switzerland, 2024, ISBN 978-3-031-52497-4. DOI: 10.1007/978-3-031-52497-4_6

[3] J. L. Bodnar, J. C. Candoré, J. L. Nicolas, G. Szatanik, V. Detalle, J. M. Vallet, Stimulated Infrared Thermography Applied to Help Restoring Mural Paintings, NDT & E International 49 (2012), pp. 40–46. DOI: 10.1016/j.ndteint.2012.03.007

[4] J. Williams, F. Corvaro, J. Vignola, D. Turo, B. Marchetti, M. Vitali, Application of Non-Invasive Active Infrared Thermography for Delamination Detection in Fresco, International Journal of Thermal Sciences 171 (2022), pp.1–13. DOI: 10.1016/j.ijthermalsci.2021.107185

[5] C. Daffara, L. Pezzati, D. Ambrosini, D. Paoletti, R. Di Biase, P. I. Mariotti, C. Frosinini Wide-band IR imaging in the NIR-MIR-FIR regions for in situ analysis of frescoes, O3A: Optics for Arts, Architecture, and Archaeology III, Munich, Germany, 17–18 June 2009, pp. 1–12. DOI: 10.1117/12.889891

[6] C. Daffara, S. Parisotto, P. I. Mariotti, D. Ambrosini, Dual mode imaging in mid infrared with thermal signal reconstruction for innovative diagnostics of the "Monocromo" by Leonardo da Vinci, Scientific Reports 11 (2021), art. nr. 22482. DOI: 10.1038/s41598-021-01837-8

[7] R. Morello, C. De Capua, A. M. Gennaro, L. Fabbiano, Characterization of material alterations in archaeological discoveries using thermography and emissivity changes, Acta IMEKO 13 (2024) 4, pp. 1–6. DOI: 10.21014/actaimeko.v13i4.1862

[8] P. Fenelli, A. De Rosa, P. Cennamo, G, Trojsi, M. Rippa, E. Gallocchio, Multidisciplinary approach of conservation of the fistulae aquariae from the archaeological site of Baiae, 2025 IMEKO TC26 International Conference on Metrology for Archaeology and Cultural Heritage, Bergamo, Italy, 15–17 October 2025, pp. 57–62. DOI: 10.21014/tc26-2025.011

[9] P. Cennamo, A. De Rosa, R. Scielzo, M. Rippa, G. Trojsi, E. Chianese, Diagnostic investigation of the wall paints conservative state in a hypogeal room of the archaeological park of Baia (Italy), Acta IMEKO 13 (2024) 3, pp. 1–8. DOI: 10.21014/actaimeko.v13i3.1807

[10] A. Di Meo, M. P. Recchia, M. Rippa, Active Thermography Analysis of Wall Paintings in the Early Christian Basilica Complex of Cimitile (Italy), 2025 IMEKO TC26 International Conference on Metrology for Archaeology and Cultural Heritage, Bergamo, Italy, 15–17 October 2025, pp. 654–658. DOI: 10.21014/tc26-2025.123

[11] C. L. K. Dandolo, P. U. Jepsen, Wall Painting Investigation by Means of Non-Invasive Terahertz Time-Domain Imaging (THz-TDI): Inspection of Subsurface Structures Buried in Historical Plasters, J Infrared Milli Terahz Waves 37 (2016) 2, pp. 198–208. DOI: 10.1007/s10762-015-0218-9

[12] K. Fukunaga, THz Technology Applied to Cultural Heritage in Practice, Springer, Tokyo, 2016, ISBN 978-4-431-55883-5.

[13] D. Giovannacci, H. C. Cheung, G. C. Walker, J. W. Bowen, D. Martos-Levif, D. Brissaud, L. Cristofol, Y. Mélinge, Time-domain

imaging system in the terahertz range for immovable cultural heritage materials, Strain 55 (2019) 2, e12292.
DOI: 10.1111/str.12292

[14] R. Radpour, N. Bajwa, J. Garritano, S. Sung, M. Balonis-Sant, (+ 4 more authors), THz imaging studies of painted samples to guide cultural heritage investigations at the Enkleistra of St. Neophytos in Paphos, Cyprus, Proc. SPIE, 9199 (2014), 91990Q.
DOI: 10.1117/12.2062228

[15] M. Bauer, K. Fukunaga, A. Keil, F. Aramini, M. Palazzo, L. Dall'Aglio, F. Friederich, Structural Investigations on Leonardo da Vinci's Mural Painting "The Last Supper" with Terahertz FMCW and TDS Techniques, Proc. of the 52nd European Microwave Conference (EuMC), Milan, Italy, 20222, pp. 808–811.
DOI: 10.23919/EuMC54642.2022.9924441

[16] F. Gennari, A. Campostrini, A. Babini, R. Lamuraglia, G. Ruocco, V. Giliberti, A. Traviglia, M. Ortolani, Preliminary Tests of Millimetric Crack Detection in Ancient Wall Paintings using a Terahertz Radar, 2025 IMEKO TC26 Int. Conf. on Metrology for Archaeology and Cultural Heritage, Bergamo, Italy, 15–17 October 2025, pp. 53–56.
DOI: 10.21014/tc26-2025.010

[17] C. Daffara, R. Fontana, M. Melchiorre Di Crescenzo, S. Scrascia, E. Zendri, Optical techniques for the characterization of surface-subsurface defects in painting layers, Proc. of SPIE, 8084:80840X (2011).
DOI: 10.1117/12.889959

[18] A. Artesani, F. Abate, R. Lamuraglia, M.A. Baldo, F. Menegazzo, A. Traviglia, Integrated Imaging and Spectroscopic Analysis of Painted Fresco Surfaces Using Terahertz Time-Domain Technique, Heritage 6 (2023) 7, pp. 5202–5212.
DOI: 10.3390/heritage6070276

[19] M. Lan, B. Li, X. Wei, X. Wu, Z. Sun, Investigation on evaluation and prediction of surface roughness and terahertz reflectivity analysis of the SiCp/Al composites component by diamond turning, Precis. Eng. 88 (2024), pp. 15–26.
DOI: 10.1016/j.precisioneng.2024.01.013

[20] I. Cacciari, S. Siano, THz characterization of corroded metals: The influence of surface roughness, 18th Italian National Conference on Photonic Technologies (Fotonica 2016), Rome, Italy, 2016, pp. 1–4.
DOI: 10.1049/cp.2016.0928

[21] I. Cacciari, S. Siano, Use of THz Reflectometry for Roughness Estimations of Archeological Metal Surfaces. J. Infrared, Millimeter, Terahertz Waves 38 (2017), pp. 503–517.
DOI: 10.1007/s10762-017-0355-4

[22] S. Mazzocato, G. Marchioro, C. Daffara, Feasibility and performance analysis in 3D printing of artworks using laser scanning microprofilometry, Acta IMEKO 11 (2022) 1, pp. 1–7.
DOI: 10.21014/acta_imeko.v11i1.1098

[23] A. Dal Fovo, J. Striova, E. Pampaloni, R. Fontana, Unveiling the Invisible in Uffizi Gallery's Drawing 8P by Leonardo with Non-Invasive Optical Techniques, Applied Sciences 11 (2021) 17, 7995.
DOI: 10.3390/app11177995

[24] R. Fontana, M. C. Gambino, M. Greco, L. Marras, M. Materazzi, E. Pampaloni, L. Pezzati, A High-Precision Surface Analysis of the Roughness of Michelangelo's David, Proc. SPIE 5146 (2003), pp. 148–159.
DOI: 10.1117/12.501252

[25] P. Carcagni, C. Daffara, R. Fontana, M. C. Gambino, M. Mastroianni, C. Mazzotta, E. Pampaloni, L. Pezzati, Optical Micro-Profilometry for Archaeology, Proc. SPIE, 5857 (2005), 58570E.
DOI: 10.1117/12.612527

[26] K. Sushil, J. Ramkumar, C. Chandraprakash, Surface roughness analysis: A comprehensive review of measurement techniques, methodologies, and modeling, Journal of Micromanufacturing 9 (2026) 1, pp. 1–25.
DOI: 10.1177/25165984241305225

[27] C. Daffara, S. Mazzocato, G. Marchioro, Multiscale roughness analysis by microprofilometry based on conoscopic holography: a new tool for treatment monitoring in highly reflective metal artworks, Eur. Phys. J. Plus 137 (2022), 430.
DOI: 10.1140/epjp/s13360-022-02605-x

[28] C. Bonifazzi, P. Carcagnì, R. Fontana, M. Greco, M. Mastroianni, (+ 4 more authors), A Scanning Device for VIS–NIR Multispectral Imaging of Paintings, Journal of Optics A Pure and Applied Optics 10 (2008) 6, pp. 1–9.
DOI: 10.1088/1464-4258/10/6/064011

[29] A. Dal Fovo, L. Maestro-Guijarro, P. M. Carmona-Quiroga, R. Fontana, F. Rosi, M. Alunni Cardinali, A. Romani, L. Comez (+8 more authors), Ageing-induced changes in varnish-coated oil paints: Surface and subsurface multi-technical analysis, Journal of Cultural Heritage 76 (2025), pp. 263–276.
DOI: 10.1016/j.culher.2025.10.003

[30] D. Porcu, S. Innocenti, J. Striova, E. Carretti, R. Fontana, Mapping Bronze Disease Onset by Multispectral Reflectography, Minerals 15 (2025) 3, pp. 1–15.
DOI: 10.3390/min15030252

[31] R. Fontana, M. Barucci, A. Dal Fovo, E. Pampaloni, M. Raffaelli, J. Striova, Multispectral IR reflectography for painting analysis, In Advanced Characterization Techniques, Diagnostic Tools and Evaluation Methods in Heritage Science. D. M. Bastidas, E. Cano, Springer, Switzerland, 2018, ISBN 978-3-319-75316-4.
DOI: 10.1007/978-3-319-75316-4_3

[32] A. Bartels, R. Cerna, C. Kistner, A. Thoma, F. Hudert, C. Janke, T. Dekorsy, Ultrafast Time-Domain Spectroscopy Based on High-Speed Asynchronous Optical Sampling, Review of Scientific Instruments 78 (2007) 3, pp. 1–8.
DOI: 10.1063/1.2714048

[33] I. Catapano, F. Soldovieri, THz imaging and data processing: State of the art and perspective, Innovation in Near-Surface Geophysics (2019), pp. 399–417.
DOI: 10.1016/B978-0-12-812429-1.00011-8

[34] I. Catapano, A. Affinito, L. Guerriero, B. Bisceglia, F. Soldovieri, Majolica imaging with THz waves: preliminary results, Appl. Phys. A (2016), pp. 122–533.
DOI: 10.1007/s00339-016-0055-2

[35] I. Catapano, F. Soldovieri, A Data Processing Chain for Terahertz Imaging and Its Use in Artwork Diagnostics, J Infrared Milli Terahz Waves (2017) 38, pp. 518–530.
DOI: 10.1007/s10762-016-0340-3

[36] R. Manca, L. Chiarantini, E. Tartaglia, F. Soldovieri, C. Miliani, I. Catapano, Non-Invasive Characterization of Maiolica Layer Structure by Terahertz Time-Domain Imaging, Coatings 13 (2023) 7, pp. 1–18.
DOI: 10.3390/coatings13071268